AIAA JOURNAL
Vol. 50, No. 2, February 2012

Improved Integral Form of the Compressible Flowfield in Thin Channels with Injection

Michel Akiki* and Joseph Majdalani†
University of Tennessee Space Institute, Tullahoma, Tennessee 37388

DOI: 10.2514/1.J051282

This work seeks to obtain an improved integral formulation for the rotational, inviscid, compressible motion in a solid rocket motor. Assuming a slender porous chamber, the method in this study reduces the problem to a single integral equation that can be solved numerically. Alternatively, closed-form analytical approximations are shown to exist for particular values of the specific heats ratio. These are obtained using an Abel transformation of the pressure equation. For the case of uniform surface mass flux, a recursion is derived for the pressure as a function of space and specific heats ratios. Here, the dependence of sidewall injection on chamber pressure is modeled according to Saint-Robert's power law. After overcoming some deficiencies encountered in previous work, results are presented and compared with two closed-form analytical solutions developed under one- and two-dimensional isentropic flow conditions for either uniformly distributed mass flux or wall injection velocity. Furthermore, agreement with an existing one-dimensional solution is established for the case of uniform mass flux. For constant sidewall injection velocity, the formulation is shown to compare favorably with a two-dimensional solution obtained by Maicke and Majdalani ("On the Rotational Compressible Taylor Flow in Injection-Driven Porous Chambers," *Journal of Fluid Mechanics*, Vol. 603, 2008, pp. 391–411). A collection of experimental data acquired by Traineau et al. (Cold-Flow Simulation of a Two-Dimensional Nozzleless Solid-Rocket Motor," AIAA Paper 1986-1447, July 1986) is also used in the validation process, including a computational fluid dynamics verification carried out using the Reynolds stress model.

Nomenclature

a	=	chamber half-height
c_p	=	constant pressure specific heat
L_s	=	sonic length (critical distance)
L_0	=	length of chamber
M	=	Mach number
m	=	injection mass flux
p	=	dimensional pressure
T	=	temperature
U_w	=	wall injection velocity
u	=	axial velocity
v	=	radial velocity
x	=	axial coordinate
y	=	coordinate normal to the propellant surface
γ	=	ratio of specific heats
ξ	=	distance from the headwall to the tip of the streamline at the sidewall
ρ	=	density
χ	=	axial coordinate referenced to the sonic length, x/L_s
ψ	=	streamfunction

Subscripts

c	=	choking conditions
w	=	wall conditions

Presented as Paper 2010-7080 at the 46th AIAA/ASME/SAE/ASEE Joint Propulsion Conference & Exhibit, Nashville, TN, 25–28 2010; received 11 March 2011; revision received 8 July 2011; accepted for publication 18 July 2011.

*Graduate Research Assistant, Department of Mechanical, Aerospace, and Biomedical Engineering. Student Member AIAA.

†H. H. Arnold Chair of Excellence in Advanced Propulsion, Department of Mechanical, Aerospace, and Biomedical Engineering; drmajdalani@gmail.com. Associate Fellow AIAA (Corresponding Author).

I. Introduction

IN THE fluid mechanics discipline, one can identify three main avenues for investigation: analytical, computational, and experimental research. Although experimental studies can require substantial investments in time and resources, computational methods can prove to be no less time consuming and laborious. And though analytical techniques can be somewhat challenging to apply, they often lead to deeper physical insight that, otherwise, cannot be gained using either of the two more common methods of investigation. In short, all three approaches remain indispensable and fundamentally interdependent. With the remarkable progress achieved in computational resources, numerical simulations have evolved to the point of granting us the ability to model complex systems, especially when implemented with a suitable set of governing equations and constitutive relations. Nonetheless, the accuracy of new computational routines remains questionable until validated in a post-predictive framework, which is often based on laboratory measurements and limiting process analytical approximations. From this perspective, it may be safe to say that the physical understanding of fundamental mechanisms underlying fluid motion can substantially benefit from theoretical analyses, such as those developed here.

Rocket propulsion, a tool on which the world's communication structure is built, stands as a field in which many advances have yet to be made, theories to be constructed, and phenomena to be explored. For example, among chemical propulsion systems, solid rocket motors are often idealized as porous chambers in which the effects of compressibility can be either retained or dismissed, depending on the gas injection speed and chamber length. In this regard, one of the most cited models remains, perhaps, Taylor's incompressible analytical representation [1], which was introduced to the aerospace community by Culick in 1966 [2]. Subsequent advances have enabled us to account for the presence of arbitrary headwall injection [3,4], wall regression [5,6], and variable chamber cross section [7]. In connection with the present study, compressible flow effects in simulated solid rocket motors have been investigated by Dunlap et al. [8], and then by Traineau et al. [9]. Both groups of investigators have conducted cold flow experiments in porous ducts in which characteristics of the spatially developing motion have been reported, including appreciable steepening beyond the incompressible

Taylor-Culick base flow [1,2]. The flattening of the mean velocity profiles, which became more pronounced as the gases advanced downstream, has prompted additional numerical simulations by Beddini [10], Baum et al. [11], Liou and Lien [12], and Apte and Yang [13]. Interest in quantifying the compressible Taylor-Culick motion and its hydrodynamic instability may also be seen in the works of Venugopal [14] and Wasistho et al. [15]. These have also attempted to simulate the compressible mean flow motion in rocket chambers under nonreactive conditions.

In the present study, we focus our attention on two theoretical techniques that have been previously considered in the treatment of this problem. The first is a variant of the Prandtl-Glauert expansion [16], first developed by Traineau et al. [9] and later revisited by Balakrishnan et al. [17], within the context of inviscid, rotational, isentropic, and compressible motion in wall-injected ducts. The technique in question invokes scaling arguments to justify the dismissal of the y-momentum equation. This step is followed by the reduction of the remaining momentum, mass, energy, ideal gas, and isentropic state relations to a single integral expression that can be solved numerically. The second technique denotes a variant of the Rayleigh-Janzen expansion. This technique was first employed by Majdalani [18] and then by Maicke and Majdalani [19] in the compressible treatment of both axisymmetric and planar chamber configurations. The attending procedure consists of expanding the governing equations in terms of a small perturbation parameter taken to be the square of the wall-injection Mach number. The resulting analysis gives rise to two explicit solutions that describe the motion of two-dimensional (2-D) compressible gases in porous chambers. At the outset, a self-similar, parameter-independent behavior is reported irrespective of the wall Mach number so long as the axial variable is rescaled by the critical distance from the headwall to the point at which sonic conditions are achieved. In this study, these models will be compared with one another and to a closed-form analytical solution representing, in the context of nozzleless rocket motors, a one-dimensional flow approximation used by Gany and Aharon [20]. The objective of this work is, hence, to reconstruct and extend the integral formulation initiated by Traineau et al. [9], such that a clear and verifiable pseudo-2-D approximation may be deduced, specifically, one that can be compared with the one- and 2-D representations obtained using asymptotic tools. It is also to provide an inversion of the integral formulation that will lead to a closed-form representation of the pressure distribution throughout the chamber.

II. Mathematical Model

A. Geometry

The domain under investigation extends horizontally from $x = 0$ to $x = L_0$ and vertically from the center axis to the wall, where the top and bottom plates may be viewed as symmetrical porous sidewalls, across which flow is injected at a velocity, $U_w(x)$. A schematic diagram of the planar chamber is given in Fig. 1.

B. Formulation

A solid rocket motor may be modeled as a slender, elongated chamber with sidewall injection [17]. Under the assumption of a low chamber aspect ratio, $a/L_0 \ll 1$, the system's conservation equations may be conveniently reduced to the following set:

$$\frac{\partial(\rho u)}{\partial x} + \frac{\partial(\rho v)}{\partial y} = 0 \qquad \text{(compressible continuity)} \tag{1}$$

$$\rho u \frac{\partial u}{\partial x} + \rho v \frac{\partial u}{\partial y} = -\frac{\partial p}{\partial x} \qquad (x\text{-momentum}) \tag{2}$$

$$\frac{\partial p}{\partial y} = 0 \qquad (y\text{-momentum}) \tag{3}$$

and

$$\rho u \frac{\partial}{\partial x}\left(c_p T + \frac{1}{2}u^2\right) + \rho v \frac{\partial}{\partial y}\left(c_p T + \frac{1}{2}u^2\right) = 0 \qquad \text{(energy)} \tag{4}$$

Note that the chamber's low aspect ratio has resulted in the dismissal of the pressure variations in the y-direction. Furthermore, the gas may be taken to be ideal with a constant, c_p, such that

$$p = \frac{\gamma - 1}{\gamma} c_p \rho T \qquad \text{(ideal gas)} \tag{5}$$

For energy conservation, Eq. (4) may be rearranged into

$$\rho u c_p \frac{\partial T}{\partial x} + \rho v c_p \frac{\partial T}{\partial y} + u\left(\rho u \frac{\partial u}{\partial x} + \rho v \frac{\partial u}{\partial y}\right) = 0 \tag{6}$$

The term that appears between parentheses stems from the left-hand side of the momentum equation. One can substitute Eqs. (2) and (5) into Eq. (6) to produce

$$\rho u\left(\frac{\partial T}{\partial x} - \frac{\gamma - 1}{\gamma}\frac{T}{p}\frac{\partial p}{\partial x}\right) + \rho v \frac{\partial T}{\partial y} = 0 \tag{7}$$

Then, inserting $\phi = T/p^{(\gamma-1)/\gamma}$ into Eq. (7), one obtains

$$\rho u \frac{\partial \phi}{\partial x} + \rho v \frac{\partial \phi}{\partial y} = 0, \qquad \rho \mathbf{u} \cdot \nabla \phi = 0, \quad \text{or} \quad \rho \frac{\mathrm{D}\phi}{\mathrm{D}t} = 0 \tag{8}$$

Because the material derivative vanishes in Eq. (8), it is clear that ϕ remains constant along a streamline.

C. Boundary Conditions

The physical requirements of the problem are used to define a consistent set of boundary conditions. These are as follows:

$$\begin{cases} u(x,a) = 0 & \text{(no slip at sidewall)} \\ u(0,y) = 0 & \text{(no headwall injection)} \\ v(x,a) = -U_w(x) & \text{(normal sidewall injection)} \\ v(x,0) = 0 & \text{(no crossflow at the centerline)} \\ T(x,a) = T_w(x) & \text{(sidewall temperature)} \\ p(0) = p_0 & \text{(headwall pressure)} \end{cases} \tag{9}$$

Note that the injection velocity and sidewall temperature vary with x, the longitudinal distance measured from the headwall.

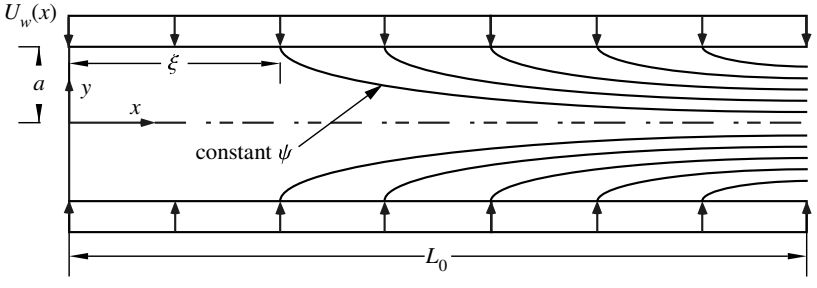

Fig. 1 Schematic diagram of a slender porous chamber.

D. Streamfunction Transformation

For planar motions, the streamfunction may be written as

$$\frac{\partial \psi}{\partial y} = \rho u, \qquad \frac{\partial \psi}{\partial x} = -\rho v \tag{10}$$

Using a constant, $(c_p T + \frac{1}{2}u^2)$, along a streamline, one can put

$$T(x,\psi) + u^2(x,\psi)/(2c_p) = T_w(\psi) \tag{11}$$

As for ϕ, the isentropic pressure-temperature relation, its value along any streamline may be set equal to its value at the sidewall. This enables us to write

$$T(x,\psi)/[p(x)]^{(\gamma-1)/\gamma} = T_w(\psi)/[p_w(\psi)]^{(\gamma-1)/\gamma} \tag{12}$$

Given that all streamlines are initiated at the injecting walls, Eq. (10) may be evaluated at $y = a$. Then, using the ideal gas expression for density, subsequent integration in the x-direction yields

$$\psi = \frac{\gamma}{(\gamma-1)c_p}\int_0^{\xi} [U_w(x)p(x)/T_w(x)]\,\mathrm{d}x \tag{13}$$

At this point, one may recognize that there exists a unique value of ψ associated with a given ξ, the distance from the headwall to the tip of a streamline taken at the sidewall. At the outset, the independent variables may be transformed from (x,ψ) to (x,ξ). When this pair is substituted into Eqs. (11) and (12), we get

$$T(x,\xi) + u^2(x,\xi)/(2c_p) = T_w(\xi) \tag{14}$$

and

$$T(x,\xi)/[p(x)]^{(\gamma-1)/\gamma} = T_w(\xi)/[p(\xi)]^{(\gamma-1)/\gamma} \tag{15}$$

Equation (13) can be readily substituted into Eq. (10) and integrated in the normal direction. This allows us to extract the coordinate, y, associated with a given position, x, and the streamline emanating from an arbitrary position, ξ, at the sidewall. We, thus, retrieve

$$y = \int_0^{\xi}\left[\frac{T(x,\xi')}{p(x)u(x,\xi')}\right]\left[\frac{U_w(\xi')p(\xi')}{T_w(\xi')}\right]\mathrm{d}\xi' \tag{16}$$

To express y in terms of the pressure only, Eqs. (14) and (15) may be straightforwardly substituted for the velocity and temperature. This operation leads to

$$y = \int_0^{\xi}\left[\frac{p(\xi')}{p(x)}\right]^{1/\gamma}\left\{1-\left[\frac{p(x)}{p(\xi')}\right]^{(\gamma-1)/\gamma}\right\}^{-1/2}\frac{U_w(\xi')}{\sqrt{2c_pT_w(\xi')}}\,\mathrm{d}\xi' \tag{17}$$

Finally, recalling that $y = a$ at $\xi = x$, Eq. (17) may be recast in the form

$$a = \int_0^{x}\left[\frac{p(\xi)}{p(x)}\right]^{1/\gamma}\left\{1-\left[\frac{p(x)}{p(\xi)}\right]^{(\gamma-1)/\gamma}\right\}^{-1/2}\frac{U_w(\xi)}{\sqrt{2c_pT_w(\xi)}}\,\mathrm{d}\xi \tag{18}$$

E. Integral Formulation with No Pressure Dependence

To simplify the analysis, three dimensionless variables $P(X)$, X, and Ξ may be introduced. These are defined by

$$P(X) = \frac{p(x)}{p_0} \tag{19}$$

$$X = \sqrt{\frac{\gamma}{\gamma-1}}\frac{1}{a}\int_0^{x}\frac{U_w(x')}{\sqrt{2c_pT_w(x')}}\,\mathrm{d}x' = \sqrt{\frac{\gamma}{2}}\frac{1}{a}\int_0^{x}M_w(x')\,\mathrm{d}x' \tag{20}$$

and

$$\Xi = \sqrt{\frac{\gamma}{\gamma-1}}\frac{1}{a}\int_0^{\xi}\frac{U_w(x')}{\sqrt{2c_pT_w(x')}}\,\mathrm{d}x' = \sqrt{\frac{\gamma}{2}}\frac{1}{a}\int_0^{\xi}M_w(x')\,\mathrm{d}x' \tag{21}$$

The preceding expressions may be inserted into Eqs. (17) and (18) to obtain

$$\frac{y}{a} = \sqrt{\frac{\gamma-1}{\gamma}}\int_0^{\Xi}\left[\frac{P(\Xi')}{P(X)}\right]^{1/\gamma}\left\{1-\left[\frac{P(X)}{P(\Xi')}\right]^{(\gamma-1)/\gamma}\right\}^{-1/2}\mathrm{d}\Xi' \tag{22}$$

and

$$\sqrt{\frac{\gamma}{\gamma-1}} = \int_0^{X}\left[\frac{P(\Xi)}{P(X)}\right]^{1/\gamma}\left\{1-\left[\frac{P(X)}{P(\Xi)}\right]^{(\gamma-1)/\gamma}\right\}^{-1/2}\mathrm{d}\Xi \tag{23}$$

Equation (23) relates the pressure and the longitudinal distance, and it must be evaluated to obtain the one-dimensional pressure distribution in the streamline coordinate system. It represents a correction to the result in Balakrishnan et al. [17]. Subsequently, Eq. (22) can be used to transform the system back to a Cartesian reference frame.

F. Integral Formulation with Pressure Dependence

One can link the mass flux at the wall, $m_w(\xi)$, to the local pressure, $p(\xi)$, by assuming a dependence on the burning-rate according to Saint-Robert's law, with a constant K and n. This can be achieved by setting

$$m_w = \rho_w U_w = Kp^n \tag{24}$$

Substituting the density obtained from the ideal gas law, the companion velocity at the wall may be expressed as

$$U_w(\xi) = \frac{\gamma-1}{\gamma}c_p\frac{T_w(\xi)}{p(\xi)}m_w(\xi) \tag{25}$$

At this point, we note that, for $n = 0$, the wall mass flux remains constant along the length of the grain. The resulting $U_w(\xi)$ may be introduced into Eq. (18) to retrieve the dimensionless forms of $P(X)$, X, and Ξ. These are

$$P(X) = \frac{p(x)}{p_0} \tag{26}$$

$$X = \sqrt{\frac{\gamma-1}{\gamma}}\frac{Kp_0^{n-1}}{2a}\int_0^{x}\sqrt{2c_pT_w(x')}\,\mathrm{d}x' \tag{27}$$

and

$$\Xi = \sqrt{\frac{\gamma-1}{\gamma}}\frac{Kp_0^{n-1}}{2a}\int_0^{\xi}\sqrt{2c_pT_w(x')}\,\mathrm{d}x' \tag{28}$$

At length, Eqs. (17) and (18) become

$$\frac{y}{a} = \sqrt{\frac{\gamma-1}{\gamma}}\int_0^{\Xi}[P(\Xi')]^{n-1}\left[\frac{P(\Xi')}{P(X)}\right]^{1/\gamma} \times\left\{1-\left[\frac{P(X)}{P(\Xi')}\right]^{(\gamma-1)/\gamma}\right\}^{-1/2}\mathrm{d}\Xi' \tag{29}$$

and

$$\sqrt{\frac{\gamma}{\gamma-1}} = \int_0^{X}[P(\Xi)]^{n-1}\left[\frac{P(\Xi)}{P(X)}\right]^{1/\gamma}\left\{1-\left[\frac{P(X)}{P(\Xi)}\right]^{(\gamma-1)/\gamma}\right\}^{-1/2}\mathrm{d}\Xi \tag{30}$$

G. Procedure

To solve this problem, one starts by integrating Eq. (30) to the extent of determining the pressure as a function of x. By numerically evaluating Eq. (29), the radial coordinate may be resolved in terms of x and ξ. With the pressure distribution at hand, the temperature may be subsequently deduced from the isentropic ratio given by Eq. (15).

The velocity may be similarly extracted from the total temperature relation given by Eq. (14).

To calculate the Mach number, the compressible flow relation, $M = u/\sqrt{(\gamma-1)c_pT}$, may be employed. In fact, the substitution of Eq. (14) into the Mach number relation renders

$$M = \sqrt{\left(\frac{2}{\gamma-1}\right)\left[\frac{T_w(\xi)}{T(x,\xi)}-1\right]} = \sqrt{\left(\frac{2}{\gamma-1}\right)\left[\left(\frac{P(\Xi)}{P(X)}\right)^{(\gamma-1)/\gamma}-1\right]} \tag{31}$$

where the right-hand side expression takes advantage of the isentropic identity realized through Eq. (15).

H. Numerical Integration

For the numerical integration of Eq. (30), the independent variable is chosen to be P, such that X may be calculated in increments of ΔP. The starting point of the iterative process may be taken at the headwall, where $X = 0$ and $P = 1$. The limiting condition occurs when $\mathrm{d}P/\mathrm{d}X \to \infty$, thus signaling the onset of choked flow. At this juncture, transforming the independent variable in Eq. (30) leads to

$$\sqrt{\frac{\gamma-1}{\gamma}}\int_P^1 (P')^{n-1}\left(\frac{P'}{P}\right)^{1/\gamma}\left[1-\left(\frac{P}{P'}\right)^{(\gamma-1)/\gamma}\right]^{-1/2} \times\left[-\frac{\mathrm{d}X(P')}{\mathrm{d}P'}\right]\mathrm{d}P' = \int_P^1 f(P')\,\mathrm{d}P' = 1 \tag{32}$$

where P and P' denote $P(X)$ and $P(\Xi)$, respectively.

To overcome endpoint singularities, the preceding integral may be split into three parts. This decomposition is intended to segregate the leftmost and rightmost cell intervals as labeled in the following manner:

$$\int_P^1 f(P')\,\mathrm{d}P' = \underbrace{\int_{P_i}^{P_{i-1}} f(P')\,\mathrm{d}P'}_{1} + \underbrace{\int_{P_{i-1}}^{1-\Delta P} f(P')\,\mathrm{d}P'}_{2} + \underbrace{\int_{1-\Delta P}^{1} f(P')\,\mathrm{d}P'}_{3} = 1 \tag{33}$$

In the region near $P = P_i$, the first integrand may be approximated by

$$\int_{P_i}^{P_{i-1}} f(P')\,\mathrm{d}P' \approx \int_{P_i}^{P_{i-1}} (P')^{n-1}\left(\frac{P'-P_i}{P'}\right)^{-1/2}\left(-\frac{\mathrm{d}X}{\mathrm{d}P'}\right)_i \mathrm{d}P' \tag{34}$$

This expression may be evaluated differently based on the value of n. We find

$$n=0:\ \int_{P_i}^{P_{i-1}} f(P')\,\mathrm{d}P' \approx 2\,\ell_n\left(\frac{\sqrt{P_i+\Delta P}+\sqrt{\Delta P}}{\sqrt{P_i}}\right)\frac{(X_i-X_{i-1})}{\Delta P} \tag{35}$$

and

$$n=1:\ \int_{P_i}^{P_{i-1}} f(P')\,\mathrm{d}P' \approx \left[P_i\,\ell_n\left(\frac{\sqrt{P_i+\Delta P}+\sqrt{\Delta P}}{\sqrt{P_i}}\right) + \sqrt{\Delta P}\sqrt{\Delta P+P_i}\right]\frac{(X_i-X_{i-1})}{\Delta P} \tag{36}$$

To compute the second integral, the trapezoidal rule may be used viz.

$$\int_{P_{i-1}}^{1-\Delta P} f(P')\,\mathrm{d}P' \approx \Delta P\left(\frac{f_1+f_{i-1}}{2}+\sum_{k=2}^{i-2} f_k\right) \tag{37}$$

where

$$f_k = \sqrt{\frac{\gamma-1}{\gamma}}(P_k)^{n-1}\left(\frac{P_k}{P_i}\right)^{1/\gamma}\left[1-\left(\frac{P_i}{P_k}\right)^{(\gamma-1)/\gamma}\right]^{-1/2}\left(-\frac{\mathrm{d}X}{\mathrm{d}P}\right)_k \tag{38}$$

In the third integral, X remains small. Consequently, $P(X)$ may be suitably expanded using a polynomial of the form

$$P(X) = 1 - \alpha X^2 + \ldots \tag{39}$$

Inserting Eq. (39) into the integral and assuming $\alpha\Xi^2 \ll 1$, we can put

$$\int_{1-\Delta P}^{1} f(P')\,\mathrm{d}P' \approx \sqrt{\frac{\gamma-1}{\gamma}}(P_i)^{-1/\gamma}[1-(P_i)^{(\gamma-1)/\gamma}]^{-1/2}\sqrt{\frac{\Delta P}{\alpha}} \tag{40}$$

To evaluate Eq. (40), it is necessary to know α. This is achieved by substituting Eq. (39) into Eq. (30) and extracting

$$\frac{1}{\sqrt{\alpha}}\int_0^X \frac{1}{\sqrt{X^2-\Xi^2}}\,\mathrm{d}\Xi = 1 \tag{41}$$

This expression enables us to deduce that $\alpha = \frac{1}{4}\pi^2$.

To sketch the numerical procedure, we make use of the linearity of Eq. (32) in X_i. Therefore, starting with $X = 0$ at $P = 1$, we solve for X_i at every step until choking conditions are reached. Choking occurs at a point where P approaches its limiting value at an infinitely steep slope where the average Mach number reaches unity. With the pressure distribution being fully determined, it may be employed in Eq. (29) and evaluated numerically. Integration returns the value of y that is needed for the complete description of the streamlines. Equations (14) and (17) can then be employed to extract the temperature and velocity.

III. Results and Discussion

In reference to the flow motion in planar porous chambers, one may consider Maicke and Majdalani [19], who were the first to construct a closed-form solution for the 2-D problem. Using a technique similar to the one applied to the cylindrical case [18], they derive a compact expression that describes the mean flowfield in a porous duct extending from the headwall to the point where fully-choked conditions are reached. For the reader's convenience, the Maicke-Majdalani model may be summarized by enumerating its key components. These are: 1) streamfunction:

$$\psi = x\sin\left(\frac{1}{2}\pi y\right) - \frac{1}{48}x\sin\left(\frac{1}{2}\pi y\right)\{\pi^2x^2[3+\cos(\pi y)] + 3[7-\cos(\pi y)]\}M_w^2 \tag{42}$$

2) centerline pressure:

$$P_c = 1 - \frac{1}{8}\gamma\pi^2x^2M_w^2 - \frac{1}{8}\gamma\left(1-\frac{3}{4}\pi^2x^2+\frac{1}{48}\pi^4x^4\right)M_w^4 \tag{43}$$

3) centerline temperature:

$$T_c = 1 + \frac{1}{8}(1-\gamma)\pi^2x^2M_w^2 + \frac{1}{96}(1-\gamma)(12-9\pi^2x^2+\pi^4x^4)M_w^4 \tag{44}$$

and 4) critical sonic distance:

$$L_s = \frac{1}{\pi M_w}\sqrt{\frac{\phi_a^{2/3}-8\phi_a^{1/3}(\gamma+1)+32(2\gamma^2+\gamma-1)}{\phi_a^{1/3}}} \tag{45}$$

where

$$\phi_a = 3\sqrt{22+18\gamma-6\gamma^2-14\gamma^3-3\gamma^4} - 128(4\gamma^3+3\gamma^2-6\gamma-14) \tag{46}$$

Another analytical solution found in the literature corresponds to a classical one-dimensional model employed by Gany and Aharon [20]. The relation in question applies to an isentropic flow with the underlying assumption that the instantaneous burning rate remains uniform along the grain, thus leading to a constant mass flux at the simulated propellant surface. The ensuing one-dimensional Mach number, pressure, and temperature may be expressed as

$$M_{1D} = \sqrt{\frac{1-\sqrt{1-\chi^2}}{1+\gamma\sqrt{1-\chi^2}}} \tag{47}$$

$$P_{1D} = (1+\gamma)^{-1}(1+\gamma\sqrt{1-\chi^2}) \tag{48}$$

and

$$T_{1D} = (1+\gamma)^{1/\gamma-1}(1+\gamma\sqrt{1-\chi^2})^{1-1/\gamma} \tag{49}$$

Concerning the calculation of the critical distance, our computation of L_s leads to a sonic length that matches, within 7%, the value predicted by Eq. (45). On this note, it should be kept in mind that, according to Majdalani [18], the critical length denotes, in the classic sense, the distance from the headwall to the point at which the centerline velocity first reaches the speed of sound. At that station, the area-averaged Mach number would not have reached unity yet. However, to reconcile with one-dimensional predictions (in which values are essentially area-averaged at a given axial station), a new definition is warranted, namely that of an area-averaged critical length, $\bar{L}_s$. Accordingly, a cross-section will be fully choked when its local average Mach number reaches unity. This condition always occurs downstream of the traditional sonic point, at $\bar{L}_s \approx 1.1L_s$.

After solving Eq. (32) in decrements of ΔP, the pressure may be reproduced as a function of the axial distance. For constant mass flux ($n = 0$), results for the central pressure and temperature are illustrated in Figs. 2a and 2b, respectively. The improved agreement between the one-dimensional expression and our model is justified by virtue of their similar boundary conditions, including the specification of uniform mass flux at the sidewall. Also shown on the graph are experimental data points acquired by Traineau et al. [9]. These researchers have considered the planar chamber with uniformly distributed mass addition.

At first glance, it may be surprising to note the improved agreement that stands between experimental measurements and the one-dimensional model. This may be attributed to the dismissal of viscous effects and other sources of damping and irreversibilities that reduce the conversion of thermal energy to kinetic motion, thus building up the pressure in the chamber. Unlike the 2-D model, in which friction leads to additional increments in irreversibilities, the one-dimensional model appears to be less susceptible to these discrepancies due to its mass injection being fundamentally axial. Also shown on the figure are numerical simulations using the RSM in a finite volume solver. The CFD data agrees with the present solution quite favorably.

The finite volume numerical simulations assume compressible viscous flow of air in a rectangular chamber. Two cases with different boundary conditions are considered. The first test case uses a constant mass flux of 13 $\mathrm{kg\,m^{-2}\,s^{-1}}$ (corresponding to $n = 0$), in a chamber of length 53 cm, height 1 cm, and a uniform mesh of 5000×100. Its results are given in Fig. 2a. The second test uses the same mesh and geometric configuration but maintains a uniform velocity profile of 4.6 $\mathrm{ms^{-1}}$ along the length of the injecting wall (corresponding to $n = 1$). Its output is given in Fig. 2c. As for the temperature boundary condition, it uses a uniform profile at the wall consisting of 400 °C. The results have been tested for consistency with higher resolution grids and different aspect ratios, thus rendering them grid independent.

Figures 2c and 2d display the results for the $n = 1$ case. The present solution seems to display excellent agreement with the analytical relations of Maicke and Majdalani [19]. The slight disparity around the choking region may be connected to the linear approximations used in the numerical procedure. These may deteriorate as the critical distance is approached. Another possible

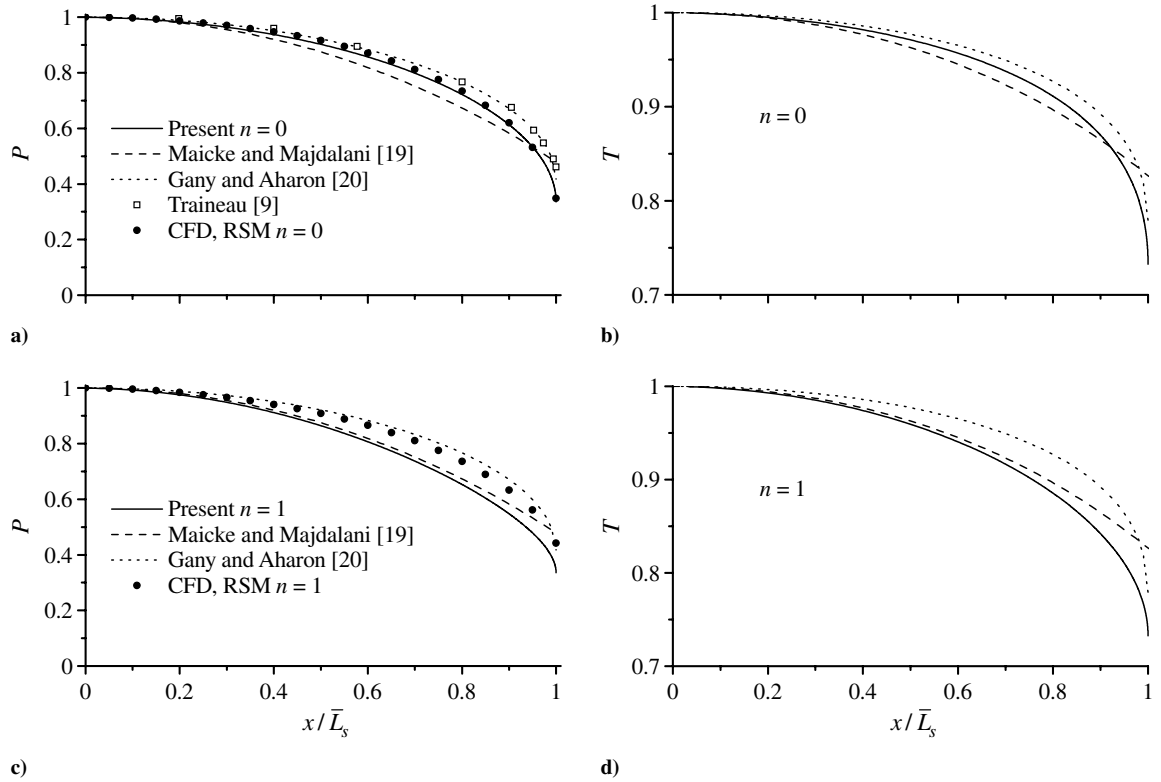

Fig. 2 Comparison between the present semi-analytical formulation and both 1D and 2D solutions by Gany and Aharon [20] and Maicke and Majdalani [19]. Also featured are experimental results due to Traineau et al. [9] and computational fluid dynamics (CFD) simulations obtained using the Reynolds stress model (RSM) in a finite volume solver. Results are shown for $\gamma = 1.4$ and $M_w = 0.05$.

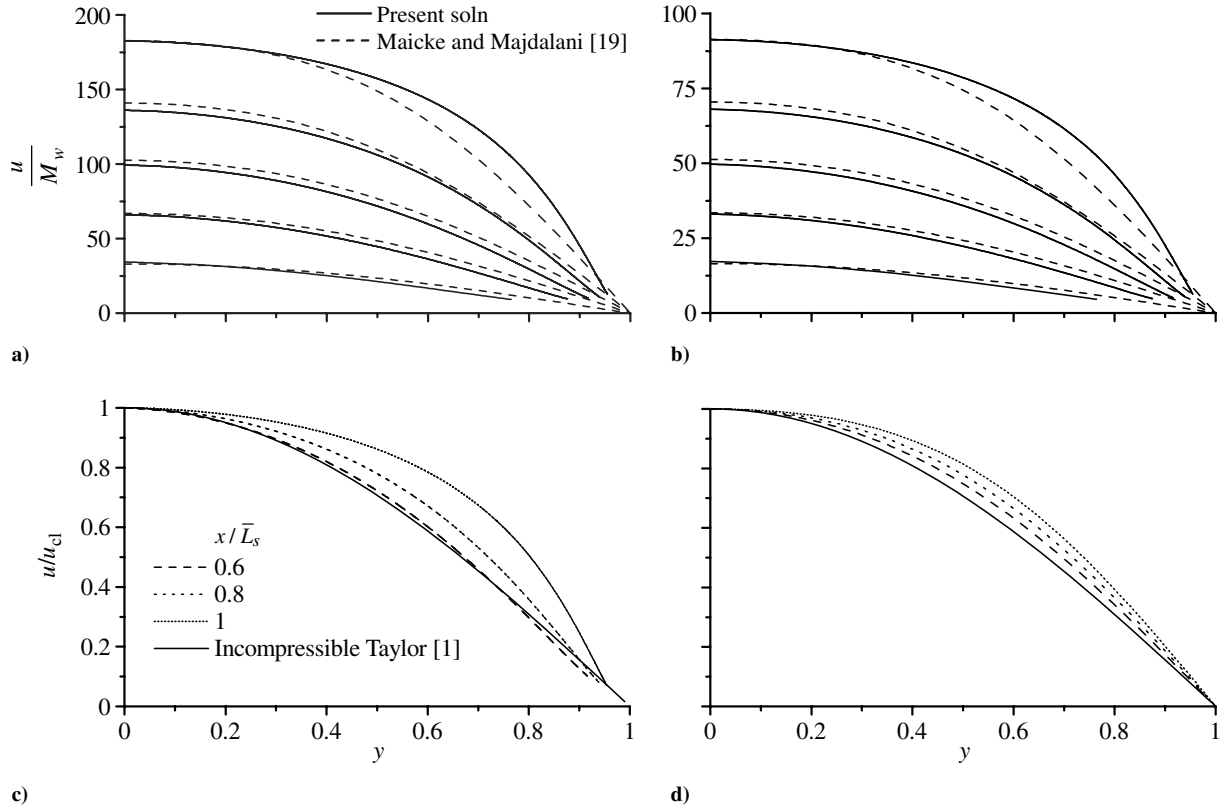

Fig. 3 Spatial evolution of the axial velocity for a) $M_w = 0.005$ and b) $M_w = 0.01$ at $x/\bar{L}_s = 0.2, 0.4, 0.6, 0.8$, and 1. Results are compared with the 2-D axisymmetric solution by Maicke and Majdalani [19]. In parts c) and d), we show the steepening of the velocity profiles when compared with the incompressible solution by Taylor [1]. The compressible profiles are due to c) the present solution and d) Maicke and Majdalani [19]. Here $\gamma = 1.4$.

justification may be attributed to the basic assumptions used in both analyses. In Maicke and Majdalani's formulation [19], the pressure, temperature, and density parameters are nondimensionalized with respect to their reference conditions at the headwall. By so doing, the analysis implies constant entropy along the length of the injecting wall, whereas in the present work, entropy is held constant along a streamline but varied along the sidewall. With the understanding that turbulence and viscous stresses become significant near the critical

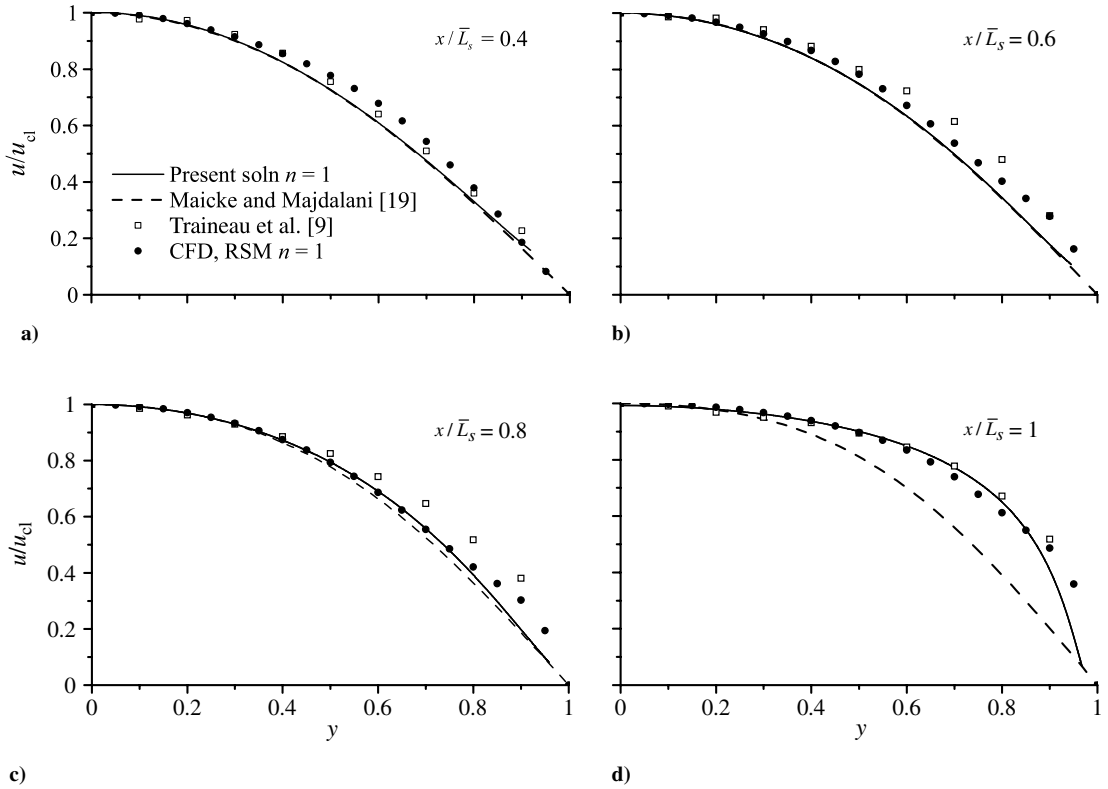

Fig. 4 Axial velocity profiles obtained using the present formulation, the analytical solution by Maicke and Majdalani [19], experimental data taken from Traineau et al. [9], and CFD simulations obtained using the RSM model in a finite volume solver.

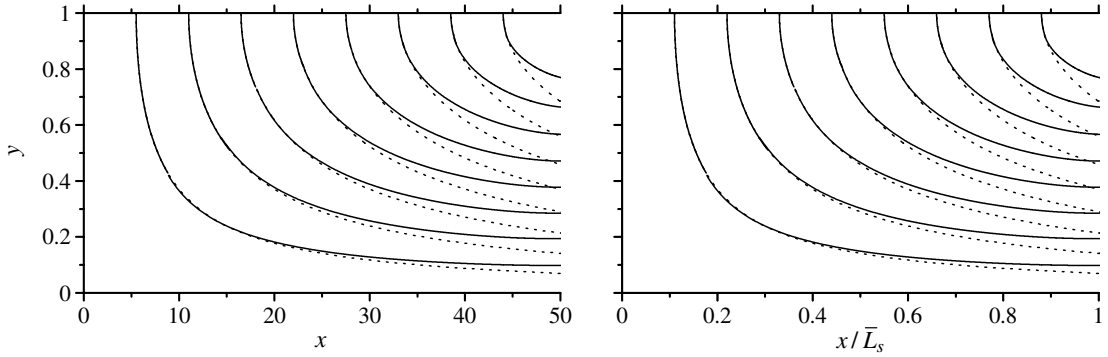

Fig. 5 Numerical streamlines for $M_w = 0.01$, using solid lines, compared with the incompressible solution by Taylor [1], using dotted lines. In b) the axial coordinate is rescaled by the critical length, thus leading to nearly perfect self-similarity.

length, dissimilarities that may be connected with differences in reversibility assumptions (i.e., homentropic versus isentropic) become magnified near the choking condition. The CFD data seem to agree with both solutions, not favoring either. On the one hand, the data points lie closer to Maicke and Majdalani's solution [19] in Fig. 2; on the other hand, the simulation exhibits a steep slope near the sonic point, as experienced in the present formulation.

The evolution of the axial velocity profile throughout the chamber is illustrated in Fig. 3 along with the 2-D analytical solution of Maicke and Majdalani [19]. As expected, the results demonstrate similar trends as the flow travels downstream. Compared with the incompressible Taylor solution, the compressible profiles display a steepening effect that is accompanied by higher velocity gradients near the wall. This steepening is also reflected in the experimental data acquired by Traineau et al. [9].

Shifting attention to Fig. 4, a favorable agreement may be reported between the present solution and Traineau's experimental data, specifically at locations where the flow remains nearly incompressible, (i.e., before the flow reaches 40% of the chamber). Advancing further downstream, steepening occurs and appears to be more pronounced in the experimental data. The disparity is justified by the dismissal of viscous and turbulence effects. These become more prominent as the flow approaches the sonic point.

Based on the numerical integration of Eq. (29), characteristic streamlines are extracted and displayed in Fig. 5. This step is carried out by first specifying a value of ξ and then integrating at discrete locations of x. At the outset, a family of coordinates is collected at a fixed value of ξ, thus leading to an assortment of points that retrace a streamline. Figure 5 also shows Taylor's incompressible solution. The comparison reveals a faster turning of the flow that may be attributed to compressibility effects. Because of the strong similarity with respect to $x/\bar{L}_s$, the ensuing graphs for any M_w become nearly identical when the axial length is rescaled, as shown in Fig. 5b.

Using Eq. (31), one can calculate the Mach number over the entire chamber. Given that the variables are expressed in terms of the axial location and a pointer for the streamline tip distance ξ, a transformation is required to revert back to Cartesian coordinates. The resulting contour plot for the local Mach numbers is presented in Fig. 6, side-by-side with the 2-D analytical predictions. The models appear to be in fairly good agreement over the entire chamber, with dissimilarity around the choking region. Note that the flow crosses $M = 1$ along a curved line rather than a point. For the sake of consistency, we therefore define choking to occur when the area-averaged Mach number reaches unity. It should be noted that Fig. 6, where the local M_w is plotted versus $x/\bar{L}_s$, will remain unchanged when the wall Mach number is varied. This is due to the geometric self-similarity with respect to $x/\bar{L}_s$ that was first proved in a 2-D axisymmetric setting by Majdalani [18].

IV. Exact Inversion Using an Abel Transformation

This section describes an analytical method used to extract expressions relating the mean pressure inside the chamber to the longitudinal distance from the headwall. The procedure we use is based on an Abel transformation, linking two functions $f(s)$ and $g(t)$, such that

$$f(s) = \int_0^s \frac{g(t)}{(s-t)^\alpha}\,\mathrm{d}t; \qquad 0 < \alpha < 1 \tag{50}$$

The inversion yields

$$g(t) = \frac{\sin(\pi\alpha)}{\pi}\frac{\mathrm{d}}{\mathrm{d}t}\int_0^t \frac{f(s)\,\mathrm{d}s}{(t-s)^{1-\alpha}} \tag{51}$$

With some algebraic manipulation, Eq. (30) can be converted into an Abel integral. This can be accomplished by taking

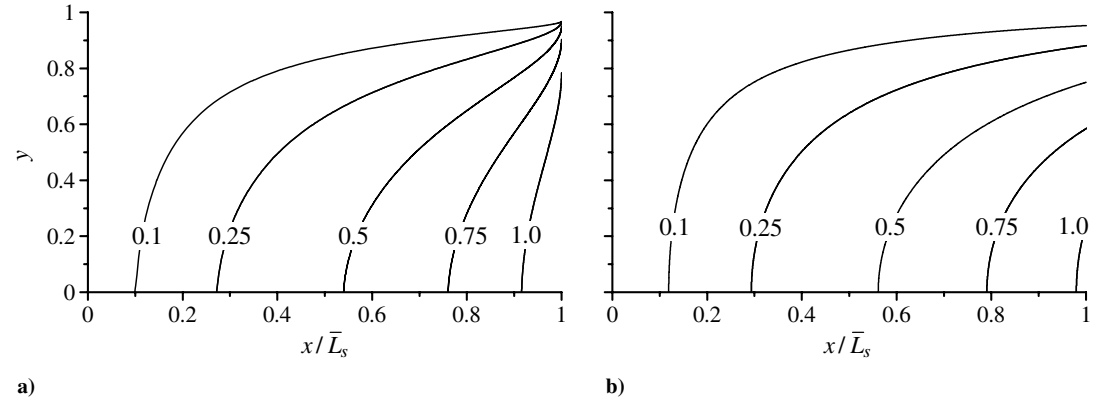

Fig. 6 Local Mach number contours for $n = 1$ according to a) numerical integration and b) analytical solution by Maicke and Majdalani [19].

Table 1 Exact solution of the pressure distribution in a simulated SRM for different values of the specific heats ratio

γ	$X(P)$
	$n=0$ (constant injection mass flux)
$[\frac{3}{2},\frac{10}{9}]$	$X=P^{\frac{1}{2(k+1)}}(\prod_{l=0}^{k-1}\frac{2l+2}{2l+1})\frac{\sqrt{1-P^{\frac{1}{k+1}}}}{\pi\sqrt{k+1}}\sum_{m=0}^{k}P^{\frac{m}{k+1}}(\prod_{l=0}^{k-m-1}\frac{2l+1}{2l+2})-\frac{\arcsin P^{\frac{1}{2(k+1)}}}{\pi\sqrt{k+1}}+\frac{1}{2\sqrt{k+1}}$
	$n=1$ (constant injection velocity)
$\frac{3}{2}$	$-\frac{2}{3\pi\sqrt{3P}}[(1+14P^{1/3})\sqrt{1-P^{1/3}}-24\sqrt{P}\arccos(P^{1/6})]$
$\frac{4}{3}$	$-\frac{4}{75\pi P^{5/8}}[(3+14P^{1/4}+148\sqrt{P})\sqrt{1-P^{1/4}}-240P^{5/8}\arccos(P^{1/8})]$
$\frac{5}{4}$	$-\frac{2}{735\pi\sqrt{5}P^{7/10}}[(75+258P^{1/5}+904P^{2/5}+8528P^{3/5})\sqrt{1-P^{1/5}}-13,440P^{7/10}\arccos(P^{1/10})]$
$\frac{6}{5}$	$-\frac{2\sqrt{2/3}}{6615\pi P^{3/4}}[(245+730P^{1/6}+1884P^{1/3}+5872\sqrt{P}+52,064P^{2/3})\sqrt{1-P^{1/6}}-80,640P^{3/4}\arccos(P^{1/12})]$
$\frac{7}{6}$	$-\frac{2}{114,345\pi\sqrt{7}P^{11/14}}[(6615+18,130P^{1/7}+40,520P^{2/7}+92,976P^{3/7}+271,808P^{4/7}$ $+2,317,696P^{5/7})\sqrt{1-P^{1/7}}-3,548,160P^{11/14}\arccos(P^{1/14})]$
$\frac{8}{7}$	$-\frac{4\sqrt{2}}{19,324,305\pi P^{13/16}}[(114,345+296,730P^{1/8}+609,980P^{1/4}+1,211,920P^{3/8}+2,607,456\sqrt{P}$ $+7,320,448P^{5/8}+60,766,976P^{3/4})\sqrt{1-P^{1/8}}-92,252,160P^{13/16}\arccos(P^{1/16})]$
$\frac{9}{8}$	$-\frac{2}{96,621,525\pi P^{5/6}}[(1,288,287+3,216,906P^{1/9}+6,261,192P^{2/9}+11,441,360P^{1/3}+21,312,640P^{4/9}$ $+44,025,600P^{5/9}+120,202,240P^{2/3}+978,421,760P^{7/9})\sqrt{1-P^{1/9}}-1,476,034,560P^{5/6}\arccos(P^{1/18})]$
$\frac{10}{9}$	$-\frac{2\sqrt{2/5}}{1,861,574,715\pi P^{17/20}}[(32,207,175+78,156,078P^{1/10}+146,371,764P^{1/5}+253,240,848P^{3/10}$ $+433,851,040P^{2/5}+775,880,960\sqrt{P}+1,558,371,840P^{3/5}+4,168,878,080P^{7/10}$ $+33,430,343,680P^{4/5})\sqrt{1-P^{1/10}}-50,185,175,040P^{17/20}\arccos(P^{1/20})]$

$$s\equiv 1-P(X)^{\frac{\gamma-1}{\gamma}},\qquad t\equiv 1-P(\Xi)^{\frac{\gamma-1}{\gamma}} \tag{52}$$

These transform Eq. (30) into Eq. (50) with

$$\begin{cases} f(s)=(1-s)^{1/(\gamma-1)} \\ g(t)=-\sqrt{\frac{\gamma}{\gamma-1}}P(\Xi)^{\gamma+3/2\gamma}P(\Xi)^{n-1}\frac{\mathrm{d}\Xi}{\mathrm{d}P(\Xi)} \end{cases} \tag{53}$$

Then, according to Eq. (51), we reap

$$g(t)=\frac{1}{\pi}\frac{\mathrm{d}}{\mathrm{d}t}\int_0^t\frac{(1-s)^{1/(\gamma-1)}}{\sqrt{t-s}}\,\mathrm{d}s \tag{54}$$

Equation (54) can be readily integrated for integer values of $1/(\gamma-1)$. The list of ratios of specific heats with physical significance include $3/2, 4/3, 5/4, 6/5, 7/6, 8/7, 9/8$, and $10/9$. For the purpose of demonstration, the analysis is carried out for $\gamma=3/2$. Evaluating the integral in Eq. (54), one gets

$$\frac{\mathrm{d}\Xi}{\mathrm{d}P(\Xi)}=\frac{1-8[P(\Xi)]^{2/3}+4[P(\Xi)]^{1/3}}{3\pi[P(\Xi)]^{n+1/2}\sqrt{3-3[P(\Xi)]^{1/3}}} \tag{55}$$

Recalling that the pressure is one-dimensional and that Ξ represents an axial distance, it is useful to replace Ξ with the axial coordinate. Integrating Eq. (55) yields

For $n=0$:

$$X=\frac{(3+8P^{2/3}+4P^{1/3})P^{1/6}\sqrt{1-P^{1/3}}-3\sin^{-1}(P^{1/6})}{3\pi\sqrt{3}}+C_1 \tag{56}$$

and

For $n=1$:

$$X=-\frac{2(1+14P^{1/3})\sqrt{1-P^{1/3}}+48\sqrt{P}\sin^{-1}(P^{1/6})}{3\pi\sqrt{3P}}+C_2 \tag{57}$$

The boundary condition at the headwall can be used to determine the constants $C_1=1/2\sqrt{3}$ and $C_2=8/\sqrt{3}$. Note that Eqs. (56) and (57) are exact solutions of our fundamental integral equation for the case where $\gamma=3/2$. After some effort, a recursive formula is developed from which expressions relating the pressure to the axial distance may be reproduced for a wide spectrum of specific heats. For $n=0$, we get

$$X=\frac{\sqrt{P^{\frac{1}{k+1}}-P^{\frac{2}{k+1}}}}{\pi\sqrt{k+1}}\left(\prod_{l=0}^{k-1}\frac{2+2l}{1+2l}\right)\sum_{m=0}^{k}\left[(P^{\frac{m}{k+1}})\prod_{l=0}^{k-m-1}\frac{1+2l}{2+2l}\right] -\frac{\arcsin P^{\frac{1}{2(k+1)}}}{\pi\sqrt{k+1}}+\frac{1}{2\sqrt{k+1}} \tag{58}$$

where $k=1/(\gamma-1)$ with integer values of k ranging between 2 and 9. For the particular case of $n=1$, the list of solutions is presented in Table 1.

V. Conclusions

In this study, an integral solution that describes the compressible gas motion in a porous chamber is reconstructed and compared with one- and two-dimensional analytical approximations obtained under isentropic flow conditions. The level of agreement is found to be commensurate with the sidewall boundary conditions associated with each of these models. In all cases, the main discrepancies occur near the sonic point and may be attributed to the various forms of approximations and linearizations affecting the integral approach. The present investigation helps to confirm the theory introduced previously in Majdalani [18], namely, the self-similarity with respect to the critical length. The study also confirms the steepening of velocity profiles and increased gradients at the sidewall due to compressibility. On the one hand, the technique presented here offers a key advantage in its ability to accommodate any sidewall injection or temperature profile, which can be later used to investigate elaborate models of the propellant-burning processes. On the other hand, the current approach requires piecewise numerical integrations, sequential inversions, and backward transformations to retrieve the original variables of interest. This procedure may render the technique laborious when compared with the simplicity with which the strictly analytical models may be implemented and resolved. Nonetheless, it remains more general and, once programmed, may entertain a variety of realistic injection patterns that may be prescribed by the problem under investigation.

Acknowledgments

This project was funded by the National Science Foundation through Grant No. CMMI-0928762. The authors wish to thank Prem Venugopal, Department of Mechanical Engineering, University of Illinois at Urbana-Champaign, for his valuable suggestions and comments.

References

[1] Taylor, G., "Fluid Flow in Regions Bounded by Porous Surfaces," *Proceedings of the Royal Society of London, Series A: Mathematical and Physical Sciences*, Vol. 234, No. 1199, 1956, pp. 456–475. doi:10.1098/rspa.1956.0050

[2] Culick, F., "Rotational Axisymmetric Mean Flow and Damping of Acoustic Waves in a Solid Propellant Rocket," *AIAA Journal*, Vol. 4, No. 8, 1966, pp. 1462–1464. doi:10.2514/3.3709

[3] Barber, T. A., Maicke, B. A., and Majdalani, J., "Current State of High Speed Propulsion: Gaps, Obstacles, and Technological Challenges in Hypersonic Applications," AIAA Paper 2009-5118, Aug. 2009.

[4] Majdalani, J., and Saad, T., "The Taylor-Culick Profile with Arbitrary Headwall Injection," *Physics of Fluids*, Vol. 19, No. 9, 2007, pp. 093601–10. doi:10.1063/1.2746003

[5] Zhou, C., and Majdalani, J., "Improved Mean Flow Solution for Slab Rocket Motors with Regressing Walls," *Journal of Propulsion and Power*, Vol. 18, No. 3, 2002, pp. 703–711. doi:10.2514/2.5987

[6] Majdalani, J., Vyas, A., and Flandro, G., "Higher Mean-Flow Approximation for a Solid Rocket Motor with Radially Regressing Walls," *AIAA Journal*, Vol. 40, No. 9, 2002, pp. 1780–1788. doi:10.2514/2.1854

[7] Kurdyumov, V., "Steady Flows in the Slender, Noncircular, Combustion Chambers of Solid Propellants Rockets," *AIAA Journal*, Vol. 44, No. 12, 2006, pp. 2979–2986. doi:10.2514/1.21125

[8] Dunlap, R., Willoughby, P., and Hermsen, R., "Flowfield in the Combustion Chamber of a Solid Propellant Rocket Motor," *AIAA Journal*, Vol. 12, No. 10, 1974, pp. 1440–1445. doi:10.2514/3.49513

[9] Traineau, J. C., Hervat, P., and Kuentzmann, P., "Cold-Flow Simulation of a Two-Dimensional Nozzleless Solid-Rocket Motor," AIAA Paper 1986-1447, July 1986.

[10] Beddini, R. A., "Injection-Induced Flows in Porous-Walled Ducts," *AIAA Journal*, Vol. 24, No. 11, 1986, pp. 1766–1773. doi:10.2514/3.9522

[11] Baum, J. D., Levine, J. N., and Lovine, R. L., "Pulsed Instabilities in Rocket Motors: A Comparison between Predictions and Experiments," *Journal of Propulsion and Power*, Vol. 4, No. 4, 1988, pp. 308–316. doi:10.2514/3.23068

[12] Liou, T., and Lien, W., "Numerical Simulations of Injection-Driven Flows in a Two-Dimensional Nozzleless Solid-Rocket Motor," *Journal of Propulsion and Power*, Vol. 11, No. 4, 1995, pp. 600–606. doi:10.2514/3.23886

[13] Apte, S., and Yang, V., "Effects of Acoustic Oscillations on Turbulent Flowfield in a Porous Chamber with Surface Transpiration," AIAA Paper 1998-3219, July 1998.

[14] Venugopal, P., "Direct Numerical Simulation of Turbulence in a Model Solid Rocket Motor," Ph.D. Dissertation, University of Illinois at Urbana-Champaign, 2003.

[15] Wasistho, B., Balachandar, S., and Moser, R., "Compressible Wall-Injection Flows in Laminar, Transitional, and Turbulent Regimes: Numerical Prediction," *Journal of Spacecraft and Rockets*, Vol. 41, No. 6, 2004, pp. 915–924. doi:10.2514/1.2019

[16] Zhiping, Z., Yongjie, N., and Qinggang, L., "Pressure Drop in Cyclone Separator at High Pressure," *Journal of Thermal Science*, Vol. 17, No. 3, 2008, pp. 275–280. doi:10.1007/s11630-008-0275-7

[17] Balakrishnan, G., Liñan, A., and Williams, F. A., "Compressible Effects in Thin Channels with Injection," *AIAA Journal*, Vol. 29, No. 12, 1991, pp. 2149–2154. doi:10.2514/3.10852

[18] Majdalani, J., "On Steady Rotational High Speed Flows: The Compressible Taylor-Culick Profile," *Proceedings of the Royal Society of London, Series A: Mathematical and Physical Sciences*, Vol. 463, No. 2077, 2007, pp. 131–162. doi:10.1098/rspa.2006.1755

[19] Maicke, B., and Majdalani, J., "On the Rotational Compressible Taylor Flow in Injection-Driven Porous Chambers," *Journal of Fluid Mechanics*, Vol. 603, No. 1, 2008, pp. 391–411. doi:10.1017/S0022112008001122

[20] Gany, A., and Aharon, I., "Internal Ballistics Considerations of Nozzleless Rocket Motors," *Journal of Propulsion and Power*, Vol. 15, No. 6, 1999, pp. 866–873. doi:10.2514/2.5509

T. Jackson
Associate Editor